Nucleic Acids Research, 2023, **51**, e111
https://doi.org/10.1093/nar/gkad953
Advance access publication date: 6 November 2023
Methods

Rapid *in situ* RNA imaging based on Cas12a thrusting strand displacement reaction

Xiaoxue Cheng[1,2,†], Xiaosong Li[1,†], Yuexi Kang[1], Decai Zhang[3], Qiubo Yu[4], Junman Chen[5], Xinyu Li[5], Li Du[1], Tiantian Yang[1], Yao Gong[1], Ming Yi[1], Songzhi Zhang[5], Shasha Zhu[1], Shijia Ding[5] and Wei Cheng[1,2,*]

[1]The Center for Clinical Molecular Medical detection, The First Affiliated Hospital of Chongqing Medical University, Chongqing 400016, P.R. China
[2]Biobank Center, The First Affiliated Hospital of Chongqing Medical University, Chongqing 400016, P.R. China
[3]Laboratory Medicine, Guangdong Provincial People's Hospital, Guangdong Academy of Medical Sciences, Guangzhou 510000, PR China
[4]Molecular Medicine Diagnostic and Testing Center, Chongqing Medical University, Chongqing 400016, P.R. China
[5]Key Laboratory of Clinical Laboratory Diagnostics (Ministry of Education), College of Laboratory Medicine, Chongqing Medical University, Chongqing 400016, P.R. China

[*]To whom correspondence should be addressed. Tel: +86 23 89011816; Fax: +86 23 68811487; Email: chengwei@hospital.cqmu.edu.cn
[†]The authors wish it to be known that, in their opinion, the first and second authors should be regarded as Joint First Authors.

Abstract

RNA *In situ* imaging through DNA self-assembly is advantaged in illustrating its structures and functions with high-resolution, while the limited reaction efficiency and time-consuming operation hinder its clinical application. Here, we first proposed a new strand displacement reaction (SDR) model (Cas12a thrusting SDR, CtSDR), in which Cas12a could overcome the inherent reaction limitation and dramatically enhance efficiency through energy replenishment and by-product consumption. The target-initiated CtSDR amplification was established for RNA analysis, with order of magnitude lower limit of detection (LOD) than the Cas13a system. The CtSDR-based RNA *in situ* imaging strategy was developed to monitor intra-cellular microRNA expression change and delineate the landscape of oncogenic RNA in 66 clinic tissue samples, possessing a clear advantage over classic *in situ* hybridization (ISH) in terms of operation time (1 h versus 14 h) while showing comparable sensitivity and specificity. This work presents a promising approach to developing advanced molecular diagnostic tools.

Graphical abstract

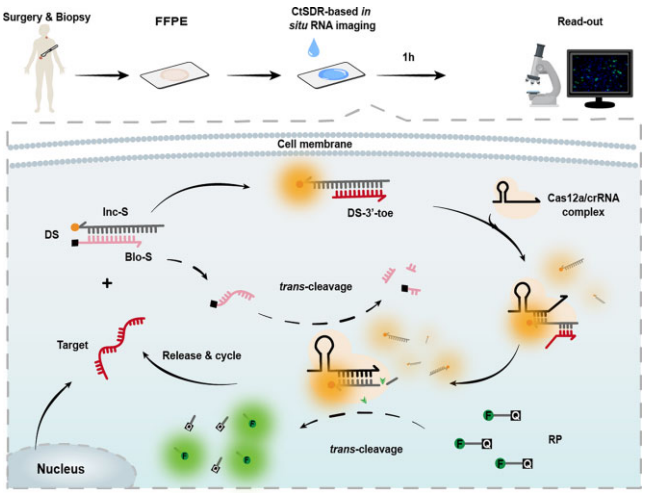

Introduction

RNA plays a critical role in the central dogma by delivering genetic and regulatory information. Its aberrant expression strongly correlates with cell proliferation, differentiation and apoptosis, thereby serving as a cancer biomarker (1–3). Sensitivity and specificity in detecting RNA are crucial for gaining insight into RNA functionality, diagnosing cancer and developing RNA-based therapies (4). Although conventional techniques such as northern blotting (5,6), reverse transcription-quantitative polymerase chain reaction (RT-qPCR) (7,8) and

Received: May 30, 2023. **Revised:** October 9, 2023. **Editorial Decision:** October 11, 2023. **Accepted:** October 12, 2023

microarrays (9,10) have significantly advanced our knowledge of RNA's roles in cancer and demonstrated the potential utility of RNA in clinical diagnostics, these methods suffer from drawbacks such as loss of temporal and spatial information, and the neglect of tumor heterogeneity (11,12). The ability to pinpoint RNA in intact cells or tissues is essential to comprehend the intricate relationship between RNA and cancer (11,13,14). Fluorescence *in situ* hybridization (FISH) allows for to resolution of the subcellular distribution of RNA molecules in fixed cells and tissues through the application of complementary probes (15). Several of these emerging FISH technologies have received a lot of attention, like π-FISH rainbow (16), RNA scope (17) and clamp FISH 1.0 and 2.0 (18,19). The π-FISH rainbow was developed with multi-fluorochromes labelled U-shaped probes to yield quantitative molecular information of RNA on cells by multi-level hybridization. Besides, the branched DNA amplification has been leveraged to enable a large number of fluorophores to target a single RNA (RNAscope). Although these techniques boast signal molecular resolution, complex and cumbersome steps such as elution and buffer replacement are required between each level, resulting in a long overall analysis time (>10 h), which is not easy to promote clinically. In addition, the abundant probes localized around the target RNA suppress the hybridization efficiency of the recognition probe to the target and fluorophores due to steric hindrance.

Strand displacement reaction (SDR), which can implement the localize amplification of the target recognition in a homogeneous phase, has emerged as a widely adopted building block for *in situ* RNA tracing and signal amplification (13,20,21). In SDR, an invader strand replaces one of the partially or fully complementary pre-hybridized strands in the substrate complex. The target-initiated SDR cycle realizes cascade signal amplification in the local homogeneous phase without multi-step operation, which shortens the analysis time and avoids steric hindrance. However, the traditional SDR is a reversible reaction, reliant upon the energy initially provided by the reactants, and the products become unavailable once the reaction reaches equilibrium. As a consequence, the efficiency of traditional SDR is limited by the energy of the initial reactants and the reaction equilibrium. To address these obstructs, multiple strategies have been explored to augment the initial energy of SDR and shift the equilibrium. The forward reaction of SDR can be regulated by adjusting the concentration of reactants or by introducing fuel chains. However, achieving maximum product yield through base pairing hybridization alone presents a formidable challenge due to the inherent constraints of double-stranded nucleic acid hybridization efficiency (22–25). Alternatively, Other research endeavors have placed emphasis on the engineering of DNA conformation by utilizing structural motifs, such as toeholds and hairpins, and subsequently developing cascade networks, namely hybridization chain reaction (HCR) (26–28) and catalytic hairpin assembly (CHA) (29–31). These networks offer an increased enthalpic contribution to the SDR process through a variety of mechanisms, including base-pairing, base-stacking and loop opening (32–35), thereby significantly accelerating the SDR process. However, the unfavorable secondary structures in these systems may influence the efficiency of SDR (36). As a result, a rapid, integrated and efficient strategy to overcome the intrinsic limitations of SDR is a big challenge, which is critical for highly efficient *in situ* RNA imaging.

In our previous study, we discovered that SDR in double-stranded DNA (dsDNA) substrate with a 3′-overhang could be triggered by a Cas12a-assisted crRNA invader, while its working principle and mechanism were still confusing (37). Combined with the principle of SDR and our previous discovery, we speculated that this popular programmable nuclease might promote SDR through some molecular mechanism. In this work, a systematic experimental analysis was conducted and demonstrated that Cas12a can dramatically thrust the efficiency of SDR in two ways: (i) the high affinity of the Cas12a/crRNA complex for the substrate can thermodynamically drive the SDR equilibrium forward; and (ii) the depletion of the by-product of SDR via the *trans*-cleavage of Cas12a drives the SDR equilibrium forward. Building upon these two mechanisms, a new Cas12a-based SDR approach, termed Cas12a thrusting SDR (CtSDR), is proposed to leverage the high affinity and trans-cleavage of Cas12a to overcome the two limitations of traditional SDR (the initiate energy and equilibrium of reaction), thereby dramatically enhancing its efficiency. Hence, a target-initiated CtSDR amplification was established for high-sensitivity and multiplex RNA detection, with order of magnitude lower LOD than the Cas13a system. Next, a rapid RNA *in situ* imaging strategy was developed and applied in cultured cells and paraffin-embedded clinical samples. Advantaged by the excellent SDR efficiency, the RNA imaging strategy possesses the immense potential to monitor microRNA expression level changes. Next, this strategy was applied for resolving the spatial distribution of viral-related two small noncoding RNA encoding regions in 66 formalin fixed paraffin-embedded (FFPE) tissues (Scheme 1). Given the comparable sensitivity and specificity of *in situ* hybridization (ISH), the CtSDR-based *in situ* imaging strategy can get rid of cumbersome steps and finish detection within 1 h. Taking advantage of the exceptional efficiency of CtSDR and high turn-over of *trans*-cleavage of Cas12a (38–40), the developed CtSDR-based *in situ* imaging strategy highlights its potential applications in molecular biology and clinical diagnostics. In addition, the combination with machine learning (ML) makes this new rapid RNA *in situ* imaging strategy possess huge application prospects for standardization of disease diagnosis.

Materials and methods

Materials and reagents

EnGen Lba Cas12a and NEBuffer 2.1/3.1/2.0/3.0 were acquired from New England Biolabs (Ipswich, MA UK). RNase inhibitor and all DNA and RNA were purchased from Sangon Biotechnology Co., Ltd. (Shanghai, China). All nucleotide sequences are shown in Supplementary Table S1-S6. Double-stranded DNAs were annealed in 1 × NEBuffer 3.0 at 80°C for 5 min and 37°C for 30 min (the molar concentration ratio of Inc-S to Blo-S was 1:1.5). 6-Mercapto-1-hexanol (MCH) was purchased from Sigma-Aldrich Chemical Co., Ltd (St. Louis, MO, USA). Bovine serum albumin (BSA) was obtained from Thermo Fisher Scientific Co., Ltd (Wilmington, USA). Tris, (2-carboxyethyl) phosphine (TCEP), diethylpyrocarbonate (DEPC) and triton X-100 were obtained from Sangon Biotechnology Co. Ltd (Shanghai, China).

Apparatus

A FS5 fluorescence spectrophotometer (Edinburgh Instruments, UK) and a 7500 real-time PCR (Thermo Fisher

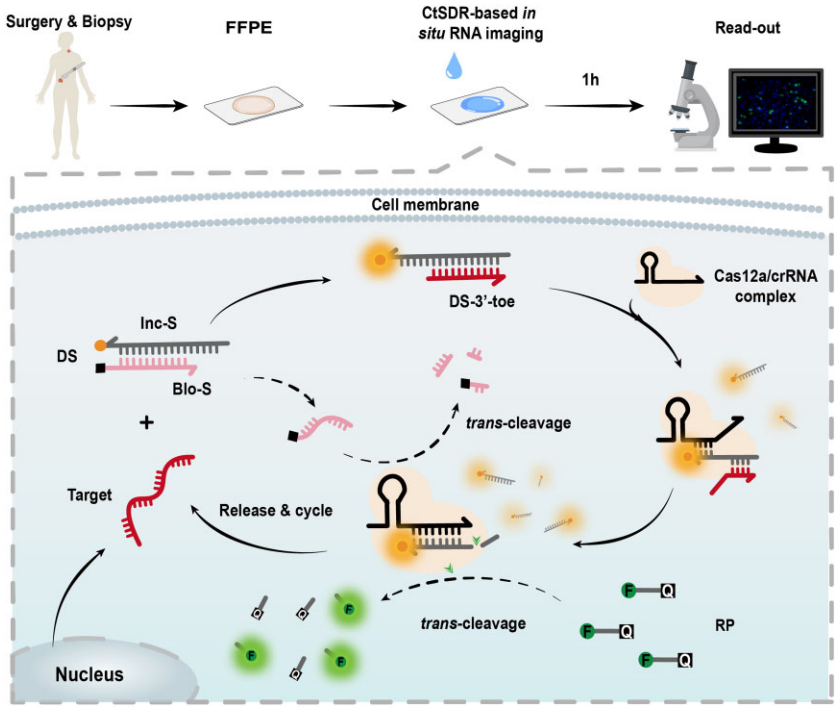

Scheme 1. Illustration of the principle of rapid *in situ* RNA imaging based on Cas12a thrusting strand displacement reaction.

Scientific, China) were utilized to obtain the fluorescence spectra, and PYX-DHS-BS-II constant temperature incubator (Hengwell, China) was used to incubate all reactions. A home-built SPR platform was used to analyze the two different SDR reactions. This SPR system was capable of simultaneously detecting multiplex targets with two separate channels and gold array chips. A red light-emitting diode (LED, 650 nm) was used as the optical source. P-polarization of the light was obtained with a sheet polarizer, and the matching liquid (n = 1.616) was mediated between the sensor chip and prism. The image reflected through the prism was captured using a 12-bit CCD camera (Retiga 1300 from QImaging). All sensorgrams were analyzed using a lab-developed program written in LabVIEW. Bio-Rad electrophoresis analyzer (Bio-Rad, USA) and Bio-Rad ChemDoc XRS (Bio-Rad, USA) were used for electrophoresis analysis. Confocal fluorescence micrographs of cells were acquired by TCS SP8 confocal laser scanning microscopy (CLSM, Leica, Germany). Flow cytometry analysis was performed using a Navios Series Flow Cytometer, 10 COLORS/3 LASER (Beckman Coulter International Trading Co., Ltd, China). The fluorescence images of clinic samples were acquired by OLYMPUS BX53 (OLYMPUS, Japan).

Insight into the mechanism of CtSDR

To explore the phenomenon of the CRISPR/Cas-promoted strand displacement reaction, Inc-S-21/ Inc-S-Cas9 and Blo-S-21/Blo-S-Cas9 were pre-annealed at a ratio of 1:1.5 to form DS-21 and DS-Cas9 in 1 × NEBuffer 3.0 at 80°C for 5 min and 37°C for 30 min. The fluorescence analysis was performed in 100 μl of the mixture containing 0.8 U/μl RNase inhibitor, 200 nM DS-21/Cas9, Cas12a/Cas9/Cas14a, crRNA-14/Inv-cr-12/Inv-cr-9, A-14 and 1 × NEBuffer 3.0. The mixture was incubated at 37°C for 60 min. The fluorescence spectra were recorded from 500–600 nm with an excitation wavelength of 492 nm for the FAM-labelled probes, and 540–650 nm with an excitation wavelength of 532 nm for the Cy3-labelled probes. The silt widths of excitation and emission were both 1.5 nm.

Measurement of the dissociation equilibrium constant (K_D)

Firstly, 20 μl thiolized DS-12(SH) (10 μM) + 180 μl KH_2PO_4 (1 M, pH 3.8) + 4 μl TCEP (500 mM) were mixed and reacted at room temperature in the dark. The surface of the gold array chip was treated with fresh piranha solution (70% H_2SO_4, 30% H_2O_2) for 10 min to eliminate the adsorbed impurities, rinsed thoroughly with ultrapure water, and finally dried with nitrogen. The DS-12(SH) (200 μl, 1 μM) was then added to the chip and incubated at 4 °C overnight. DS-12(SH) could be assembled onto the gold chip via Au-S bonds. Next, BSA (1%) and MCH (1%) were incubated with the chip for 1 h and 30 min, respectively. After washing with ultrapure water and drying with nitrogen, the chip was docked into the SPR instrument for further use. At the start, 1 × NEBuffer 3.0 was injected into the instrument at a speed of 5 μl min^{-1}. After the instrument reached a steady state, the Cas12a/crRNA complex or crRNA was injected at a speed of 50 μl min^{-1}. After 2 min 40 s, the injection was suspended to ensure sufficient hybridization time for the Cas12a/crRNA complex or crRNA to the DS-12(SH). When the SPR signal stabled again, the speed was slowed down to 5 μl min^{-1} to wash away the non-specific binding components.

The influence of location and length of toehold in CtSDR

To explore the phenomenon of the CRISPR/Cas-promoted strand displacement reaction, Inc-S-3′/ Inc-S-5′ and Blo-S-3′-n/Blo-S-5′-n were pre-annealed at a ratio of 1:1.5 to form DS-3′-toe-n and DS-5′-toe-n (n = 2, 3, 4, 5, 6, 7 and 8). RT-PCR analysis was performed in a 50 μl mixture comprising 1 μM

RP, 0.8 U/μl RNase inhibitor, 100 nM DS-3′-toe-n and DS-5′-toe-n, Cas12a and crRNA, and 1 × NEBuffer 3.0. The assay was carried out using 7500 real-time PCR (Thermo Fisher Scientific, China) at 37°C for 60 min. Fluorescence signals emitted from FAM and Cy3 were collected by the FAM and Cy3 channels, respectively, at the end of every cycle, with each cycle sustained for 1 min.

End-point fluorescence analysis was performed in 100 μl of the mixture containing 500nM RP, 0.8 U/μl RNase inhibitor, 20 nM DS-3′-toe-n and DS-5′-toe-n, Cas12a and crRNA, and 1 × NEBuffer 3.0. The mixture was incubated at 37°C for 60 min. The fluorescence spectra were recorded from 500 to 600 nm with an excitation wavelength of 492 nm for the FAM-labelled probes, and 540–650 nm with an excitation wavelength of 532 nm for the Cy3-labelled probes. The silt widths of excitation and emission were both 1.5 nm.

Fluorescence analysis for miRNA detection

Fluorescence analysis was performed in 100 μl mixture containing 20 nM Cas12a, 10 nM crRNA, 10 nM Target, 10 nM DS, 500 nM RP, 0.8 U/μl RNase inhibitor and 1 × NEBuffer 3.0. This mixture was incubated at 37 °C for 1 h before the fluorescence measurements. The fluorescence spectra were recorded from 500–600 nm with an excitation wavelength of 492 nm for the FAM-labelled probes, and 540–650 nm with an excitation wavelength of 532 nm for the Cy3-labelled probes. The silt widths of excitation and emission were both 1.5 nm.

Native polyacrylamide gel electrophoresis

To confirm the feasibility of our method, the products and components of Cas12a were studied using 12% native polyacrylamide gel electrophoresis (PAGE) in 1 × TBE running buffer (89 mM Tris-boric acid, 2 mM EDTA, pH 8.3) at 120 V constant voltage for 40 min. The gels were imaged using a gel image system after Gold View (GV) staining for 20 min at room temperature and a ChemiDoc XRS$^+$ imaging system (Bio-Rad). The concentration of reactants in every lane was 1μM.

Cell culture

The breast cancer cell line MCF-7 and normal breast cell line MCF 10A were obtained from American Type Culture Collection (ATCC, Manassas, VA, USA). MCF-7 cells were cultured in Dulbecco's modified eagle medium (DMEM; Gibco, MA, USA) supplemented with 10% fetal bovine serum (FBS; Gibco, MA, USA). MCF 10A cells were cultured in a special medium obtained from Procell (Wuhan, China). All cells were incubated in a humidified incubator at 37°C with 5% CO_2.

Intracellular RNA imaging

MCF-7 and MCF-10A cells at a density of 1.0 × 10^6 were fixed with fix solution (methanol: acetic acid = 3:1) for 20 min at room temperature. After fixation, the cells were permeabilized with 1 × PBS containing 0.5% v/v Triton-X 100 at 37°C for 5 min. Subsequently, the cells were washed three times with 1 × PBS (each wash lasting 1 min) at 37°C. Incubation of the CtSDR system was conducted in a 10 μl mixture at 37°C for 1 h. This mixture contained 20 nM Cas12a, 10 nM crRNA, 10 nM target, 10 nM DS, 500 nM RP, 0.8 U/μl RNase inhibitor and 1 × NEBuffer 3.0. After probe incubation, DAPI was used to stain the cells prior to confocal imaging.

Cell transfection

To silence miR-21 and miR-155, miR-21 and miR-155 inhibitors were synthesized by Sangon Biotechnology Co., Ltd (Shanghai, China). A mimic of miR-155 was also obtained from Sangon Biotechnology Co., Ltd (Shanghai, China) to overexpress miR-155. Lipo6000™ Transfection Reagent (Beyotime Biotechnology, Shanghai, China) was used for cell transient transfection following the manufacturer's instructions.

Total RNA isolation and reverse transcription PCR (RT-PCR)

A universal microRNA purification kit (EZBioscience, USA) was used to extract the total RNA from breast cancer cell lines (MCF7 and MCF10A) following the manufacturer's recommendations. Following reverse transcription with the miRNA First Strand cDNA Synthesis (Tailing Reaction) kit (Sangon Biotech, Shanghai, China), miR-21, miR-155 and U6 expression patterns were detected via RT-PCR with BlasTaq™ 2X qPCR MasterMix (Applied Biological Materials Inc., Canada) in accordance with the manufacturer's instructions. The expression of mRNA was assessed by relative quantification using the $2-\Delta\Delta Ct$ method. The U6 expression level used to normalize the expression levels of miR-21 and miR-155.

Flow cytometry

MCF7 and MCF10A cells were seeded in a 12-well plate and incubated overnight to 80−90% confluency. After cell transfection, the cells in each well were detached from the plate using 0.25% trypsin and washed with 1 × PBS three times. MCF-7 and MCF-10A cells at a density of 1.0 × 10^6 were fixed with fix solution (methanol: acetic acid = 3:1) for 20 min at room temperature. After fixation, the cells were permeabilized with 1 × PBS containing 0.5% v/v Triton-X 100 at 37°C for 5 min. Subsequently, the cells were washed three times with 1 × PBS (each wash lasting 1 min) at 37°C. Incubation of the CtSDR/cSDR system was conducted in a 100 μl mixture containing 2 μM Cas12a, 1μM crRNA-21/155, 1 μM DS-21/155, 10 μM RP, 0.8 U/μl RNase inhibitor and 1 × NEBuffer 3.0 at 37°C for 1 h. After being processed for intracellular miRNA imaging, the cells were maintained in 1 × PBS on ice in the dark for flow-cytometry measurements. In total, 10^6 cells were analyzed per sample. Fluorescein isothiocyanate (FITC) represents the *trans*-cleavage activity of Cas12a, Cy3+ represents microRNA-21 in MCF7 cells, and PerCP + represents microRNA-155 in MCF7 cells. Flow cytometry analysis was performed using a Navios Series Flow Cytometer, 10 COLORS/3 LASER (Beckman Coulter International Trading Co., Ltd, China).

In situ imaging of clinical tissue samples

For further investigation, biopsy specimens with sufficient tissue and clinical data were retrieved from the Department of Pathology of the First Affiliated Hospital of Chongqing Medical University. This study was approved by the Ethics Committee of the First Affiliated Hospital of Chongqing Medical University (2022-K461). *In situ* hybridization for Epstein–Barr encoding region (EBER) was performed on formalin-fixed,

paraffin-embedded tissue sections using an EBERs assay kit (ZSGB-BIO, China). All tissue samples were maintained at 40°C for 30 min and then deparaffinized, dehydrated, digested with pepsase and hybridized at 37°C for 1 h with 10 μl reaction mix containing Cas12a, crRNA-E1, crRNA-E2, DS-E1, DS-E2 (both 1 μM) and RP (10 μM). DAPI was used to stain the cells prior to fluorescence imaging.

Results

Mechanism of cas12a thrusting SDR (CtSDR)

In the context of traditional toehold-mediated SDR(TSDR), a double helix exchanges one of its strands with an incoming complementary invader strand to form a more stable duplex. To gain deeper insights into the underlying mechanism of CtSDR, two different SDR models were devised: crRNA-mediated SDR (cSDR) and CtSDR (Figure 1A and B). A ds-DNA with a toehold (denoted as DS-12), was employed as the substrate of TSDR, which was formed by Cy3-labelled Inc-S-12 (gray strand, Supplementary Table S1) and BHQ2-labelled Blo-S-12 (pink strand, Supplementary Table S1). Due to Förster resonance energy transfer (FRET), the fluorescence of DS-12 remained in the 'off' state. With or without the assistance of Cas12a protein, crRNA (Inv-cr-12, Supplementary Table S1) could act as the invading strand to displace Blo-S-12 and bind with Inc-S-12 by TSDR, ultimately resulting in the recovery of the fluorescence signal. Thus, the fluorescence change could indicate the SDR efficiency. As displaced in Figure 1C, CtSDR achieved an approximately 4.8-fold increase in fluorescence intensity (FI) compared to cSDR, demonstrating that Cas12a enhances the efficiency of SDR.

$$\mathrm{I} + \mathrm{S} \underset{k_r}{\overset{k_f}{\rightleftharpoons}} \mathrm{B} + \mathrm{P}$$

$$\sqrt{\frac{k_f}{k_r}} = e^{-\Delta G/2RT} \tag{1}$$

$$K_D = \frac{k_r}{k_f} \tag{2}$$

$$\Delta G = RTln\left(K_D\right) \tag{3}$$

For the reaction I + S→B + P (invading strand + substrate → blocking strand + product), k_f is the forward reaction rate constant for SDR, while k_r is the corresponding rate constant for the reverse reaction. According to Equations (1–3), the standard free energy change of hybridization (ΔG) correlates with the corresponding dissociation equilibrium constant (K_D) (41). Next, to investigate the kinetic variations of the Cas12a/crRNA complex and crRNA as invading strand towards the substrate, surface plasmon resonance (SPR) was employed. As shown in Figure 1D and E, thiol-modified DS-12 was jointed on the surface of the gold chip by Au-S bond. The concentration-dependent curves of the Cas12a/crRNA complex and crRNA towards DS-12 were obtained to quantify the corresponding K_D. The K_D of the Cas12a/crRNA complex was more than one order of magnitude lower than that of single crRNA, indicating the significantly increased affinity of the Cas12a/crRNA complex towards the substrate. This effect might due to the hydrogen bonding and ionic interactions between backbone phosphate groups and Cas protein (42,43). Since the increased affinity results in a larger absolute value of ΔG, allowing CtSDR to undergo a more thorough forward reaction thermodynamically than cSDR and thereby offering enhanced reaction efficiency. Based on the propulsion of Cas12a, the ratio of Cas/crRNA complex to substrate was optimal as 1:1 to obtain optimal CtSDR performance (Supplementary Figure S2).

In addition to enhanced affinity, we speculated that *trans*-cleavage of the displaced incumbent strand would positively affect SDR. In order to confirm this hypothesis, two groups of experiments were carried out. In the first group, Cas9, a CRISPR-associated protein without *trans*-cleavage activity(44), was used to promote SDR by improving the affinity between the invading crRNA and substrate. In the second group, Cas12a was used to promote SDR via improved affinity and *trans*-cleavage of the displaced incumbent strand. As depicted in Figure 1F and G, Cas9 in the first group experiments shows an obvious but weak improvement of FI ($\Delta FI_{II\text{-}I} = 8.24E + 3 \pm 9.52E + 2$), indicating limited reaction promotion. In contrast, Cas12a in the second group experiments more remarkable improved FI ($\Delta FI_{II\text{-}I} = 1.95E + 4 \pm 8.6E + 2$), indicating that Cas12a acts as a superior SDR helper due to its *trans*-cleavage activity. Next, we added an extra Cas14a system to each group of experiments. Cas14a, which is triggered by an uncorrelated activator, served as a collateral ssDNA scissor to compensate for the missing *trans*-cleavage in the Cas9 system(45). Surprisingly, FI in the first group dramatically improved with the auxiliary Cas14a system ($\Delta FI_{III\text{-}II} = 2.25E + 4 \pm 1.07E + 3$), supporting our assumption that *trans*-cleavage of the displaced blocking strand can promote SDR. Contrarily, FI improvement with the Cas14a system in the second group was quite limited ($\Delta FI_{III\text{-}II} = 4.89E + 3 \pm 1.38E + 3$) because the collateral cleavage of Cas12a itself was already saturated and guaranteed highly effective SDR ($FI_{II} \approx FIIII \approx FI_{III}$). These results indicate that depleting the displaced blocking strand via *trans*-cleavage of Cas12a can drive the equilibrium forward and further improve the efficiency of SDR. Given the depletion effect of Cas12a towards the blocking strand, the amount of blocking strand in the pre-annealed substrate was studied in Supplementary Figure S3. The results proved that In-S: Blo-S ≤ 1 could cause severe signal leakage, and In-S: Blo-S > 1 could slightly consume the *trans*-cleavage activity of Cas12a. To eliminate the possibility of signal leakage, we discard some of the *trans*-cleavage activity of Cas12a in exchange for better occlusion of substrate, so the In-S: Blo-S = 1:1.5 was adopted in all experiments.

Taken together, these results demonstrate that Cas12a can dramatically promote the efficiency of SDR. Its mechanism was confirmed to be: (i) the elevated affinity of Cas12a/crRNA towards the substrate confers increased energy to the reaction, resulting in a thermodynamically favorable drive of the SDR equilibrium; and (ii) the consumption of SDR by-product via the *trans*-cleavage of Cas12a, which facilitates the promotion of the SDR equilibrium in a forward direction.

Effects of toehold length and displacement direction on the kinetics of CtSDR

Prior research has demonstrated that the helicase activity of Cas12a is directional(42), and the rate of SDR can be tuned by modifying the length of the toehold(32,46). To assess These influences on the effectiveness of SDR, two sets of substrates

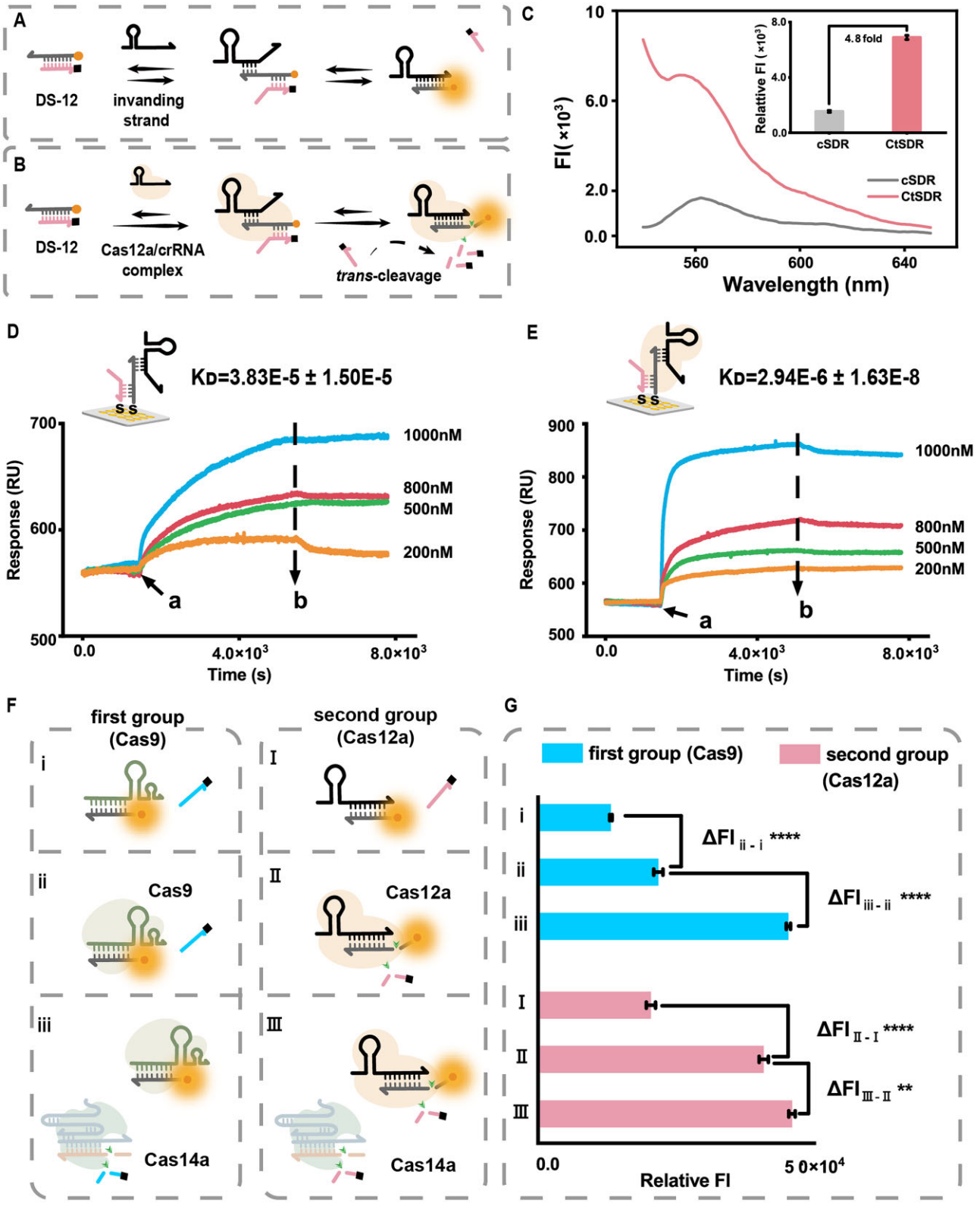

Figure 1. Illustration of cSDR **(A)** and CtSDR **(B)**. **(C)** The fluorescence curves for cSDR (black line) and CtSDR (red line). 0.8 U/μl RNase inhibitor, 100 nM DS-12, Cas12a and crRNA, and 1 × NEBuffer 3.0, recorded by FS5 fluorescence spectrophotometer. **(D)** Typical SPR sensorgrams of CtSDR with different Cas12a/crRNA complex concentrations (1000, 800, 500, 200 nM). 1 μM DS-12(SH), and 1 × NEBuffer 3.0. **(E)** Typical SPR sensorgrams of cSDR with different crRNA concentrations (1000, 800, 500, 200 nM): 'a' shows the timepoint of reactant injection, and 'b' shows the timepoint of washing. 1 μM DS-12(SH), and 1 × NEBuffer 3.0. The corresponding K_D values were evaluated with TraceDrawer. **(F)** Illustration of cSDR, CtSDR, and CtSDR-aCas14a of the Cas9 system (first group), Cas12a system (second group), and corresponding normalized FI of Cy3 **(G)**, respectively. Error bars represent standard deviations of three independent experiments **** $t < 0.0001$, ** $t < 0.01$. 0.8 U/μl RNase inhibitor, 200 nM DS-21/DS-Cas9, 200 nM Cas12a/Cas9/Cas14a, 200 nM crRNA-14/Inv-cr-12/Inv-cr-9, 200 nM A-14 and 1 × NEBuffer 3.0, recorded by FS5 fluorescence spectrophotometer.

for CtSDR and cSDR reaction models were designed with different toehold lengths and locations. The toehold length varied from 2 to 8 nucleotides and the toehold position located either at the 3′ or 5′ end of the substrate (the substrates, named DS-3′-toe-n and DS-5′-toe-n, were formed by Inc-S-3′/ Inc-S-5′ and Blo-S-3′-toe-n/ Blo-S-5′-toe-n, $n = 2, 3, 4, 5, 6, 7, 8$, respectively. Supplementary Table S2, Supplementary Figure S1). The differences in SDR efficiency between cSDR and CtSDR could be monitored by recording the change in fluorescence of Cy3. In addition, a FAM/BHQ1-labelled ssDNA report probe (RP) was introduced to the CtSDR system to further assess the *trans*-cleavage activity of Cas12a, which was triggered in CtSDR (Figure 2A). Given the mechanism (ii) of CtSDR was studied under no RP situation, we verified whether the addition of RP would affect the effect of CtSDR. As shown in Supplementary Figure S4, adding RP could slightly consume the *trans*-cleavage activity of Cas12a by the competitive effect (competed as substrate with Blo-S-3′-toe-n/ Blo-S-5′-toe-n), which further proved the mechanism (ii) of CtSDR. However, we still used RP in the following experiments for two reasons. In one aspect, the RP was the signal reporter that could not be omitted. In another part, the degree of signal reduction by RP was acceptable.

As depicted in Figure 2B, the FI signal increased along with the toehold base number increasing in the two displacement location groups(3′-toe and 5′-toe), which was consistent with prior research (46,47). When the toehold base number was less than 4, no significant change in FI was observed. however, when the toehold base number was 4 to7, the 3′-toe group (CtSDR-3′-toe and cSDR-3′-toe) had a higher signal increase than the 5′-toe group (CtSDR-5′-toe and cSDR-5′-toe). Notably, an almost equal FI was observed in the 3′-toe group and the 5′-toe group when the toehold base number was 8. These effects might be due to the SDR proceeding in a low-efficient manner when the toehold base number is less than 4, and spontaneous dissociation of the substrate exists when the toehold base number is 8 (47). The CtSDR-triggered *trans*-cleavage toward RP was also investigated, and the results exhibited a similar trend to that of Figure 2B, suggesting that the *trans*-cleavage activity of Cas12a was related to SDR efficiency in CtSDR (Figure 2C). Therefore, the 3′-toe was selected for further experiments. Next, real-time fluorescence experiments were performed to monitor FI changes in CtSDR and cSDR with DS-3′-toe-n, $n = 4–8$. As shown in Figure 2D, the DS-3′-toe with 4 and 5 toeholds in the CtSDR system realized an obvious increase in fluorescence. Moreover, fluorescence recovery was more significant when the toehold was increased to 6–8. And the decrease in CtSDR-3′-toe-7/8 might be due to the massively accumulated cleaved short strand (Cy3-labelled short strands and BHQ2-labelled short strands) forming a short double strand with the reaction processing. The rate constant (k_{rep}) of CtSDR calculated using MATLAB indicated an increase of orders of magnitude relative to cSDR (Supplementary Table S7, MATLAB code in SI). By tuning the toehold base number, the rate of SDR varied by orders of magnitude (24). Notably, the CtSDR-triggered *trans*-cleavage showed the same trend as cSDR (Figure 2E). The initial rate constant (V_0) also displayed an increase of orders of magnitude along with an increase in the base number (Supplementary Table S8). Ultimately, the DS-3′-toe with a toehold base number of 7 was optimized as the displacement substrate to further explore the applications of CtSDR in RNA molecular diagnosis.

CtSDR-based RNA analysis

Having validated the mechanism of CtSDR, we then explored its applications in the area of molecular diagnosis. To do so, a target-initiated CtSDR amplification was developed for ultrasensitive molecular diagnosis. As depicted in Figure 3A, the RNA target was employed to displace the Blo-S-21 (the pink strand, Supplementary Table S3) and hybridized with Inc-S-21 (the gray strand, Supplementary Table S3) to form DS-3′-teo-7–21 and restoration the fluorescence of Cy3 via toehold exchange, in which the Blo-S-21 served as blocking strand prevented signal leak and indicating the target recognition by FRET effect. The Cas12a/crRNA complex subsequently recognized DS-3′-teo-7–21, initiating the CtSDR process and restoring FAM fluorescence through *trans*-cleavage. Simultaneously, the displaced free target could enter the next cycle to achieve cascade amplification of the readout. While the free Blo-S-21 would be hydrolyzed by the *trans*-cleavage of Cas12a, propelling reaction forward. First, we verified the efficiency of activating Cas12a's *trans*-cleavage property with DS activator (Supplementary Figure S6). And the result showed DS activator could reach around 80% efficiency of the ssDNA activator.

MicroRNA-21 (miR-21) was adopted as the target to evaluate the feasibility of this assay by inspecting the fluorescence signal in the Cy3 channel. As shown in Figure 3B, the similar FIs between curves 1 and 3, 2 and 4, indicated no leakage in the designed strategy. In addition, the target-initiated CtSDR (curve 5) showed approximately 5-fold fluorescence recovery compared to the target-mediated SDR (curve 2) and target-initiated cSDR (curve 4), suggesting that the Cas12a/crRNA complex remarkably enhanced the efficiency of SDR. Meanwhile, a low concentration of the target could trigger the CtSDR reaction, proving the target recycle for cascade amplification (Supplementary Figure S7). Subsequently, we evaluated the *trans*-cleavage of Cas12a activated by the target-initiated CtSDR by inspecting the fluorescence signal in the FAM channel. As depicted in Figure 3C, an extremely high peak was acquired (red line), implying the feasibility of the proposed miRNA detection approach. Then, the 12% PAGE analysis was performed to characterize target-initiated CtSDR (Figure 3D). The new bright band in lane 6 suggested the successful preparation of the partially complementary dsDNA substrate. Compared with line 4, a slightly up-shifted band was observed in lines 7 and 9, indicating the feasibility of target-initiated SDR and target-initiated cSDR. Lane 11 showed clear degradation of nonspecific ssDNA substrates, implying that adding a target could initiate *trans*-cleavage of Cas12a towards ssDNA substrates, suggesting the ability of CtSDR to activate the *trans*-cleavage of Cas12a. Another target, miR-155 and the corresponding SDR and trans-cleavage systems were also synthesized to verify the universality of target-initiated CtSDR (Supplementary Figure S8). By programming the crRNA and DS substrate, our proposed method possesses good universality for different targets. The above consistent results confirmed that target-initiated CtSDR amplification possesses high efficiency and universality.

The substrate of different conformation, including hairpin (HP) and DS, was first investigated to obtain a better reaction efficiency (Supplementary Figure S9a and b). Similarly, after optimizing HP with a range of toeholds (Supplementary Table S4, Supplementary Figure S5 and S9c), the DS conformation still exhibited an 8-fold signal-to-noise ratio (S/N) compared with HP (Supplementary Figure S9d). Then,

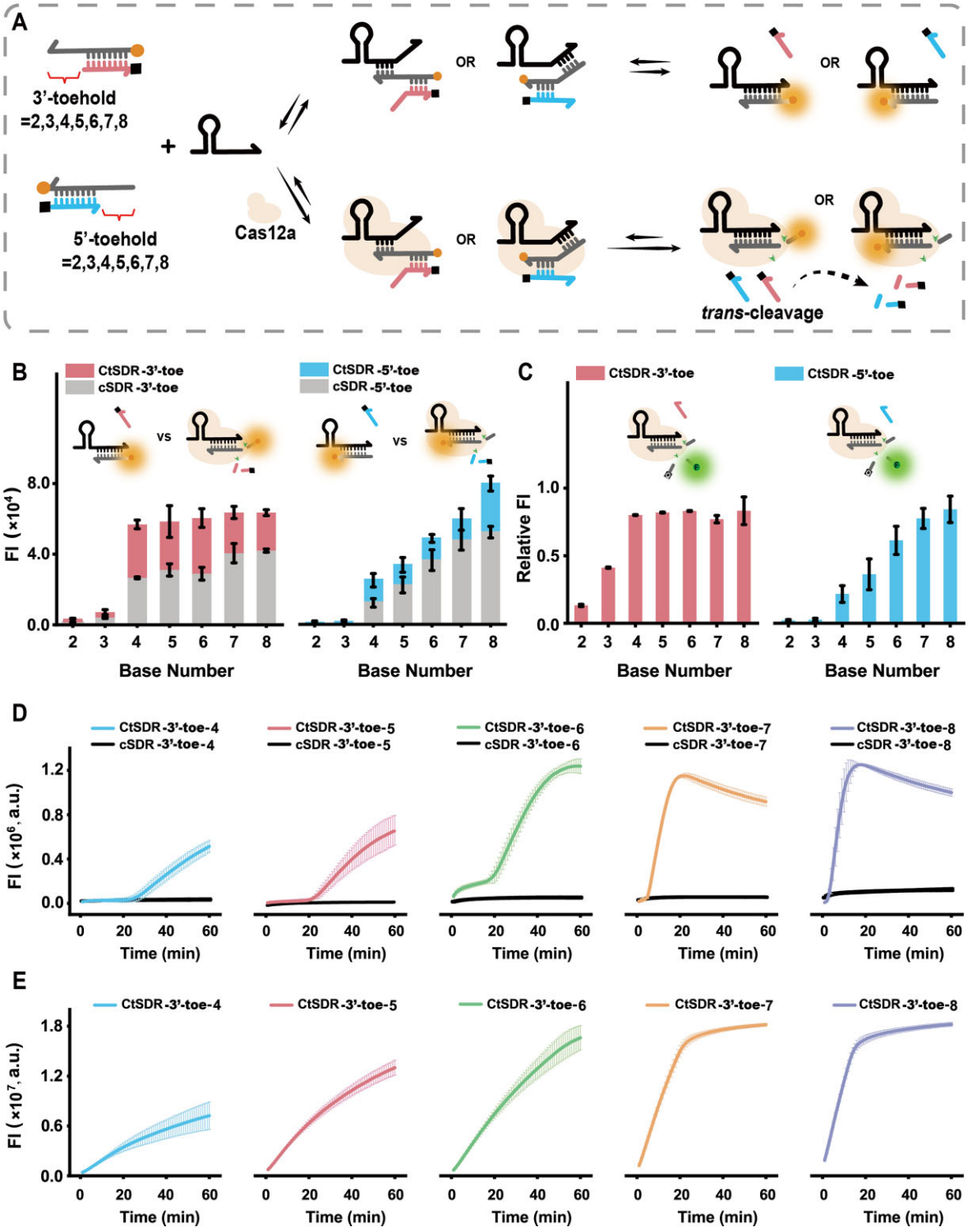

Figure 2. (A) Illustration of cSDR and CtSDR with different displacement directions and toehold base numbers. **(B)** The FI of Cy3 produced by cSDR and CtSDR with different toehold lengths (range from 2 to 8) and locations (3′-toe and 5′-toe), and **(C)** the FI of FAM produced by the *trans*-cleavage of CtSDR with different toehold lengths (range from 2 to 8) and locations (3′-toe and 5′-toe). 500 nM RP, 0.8 U/μl RNase inhibitor, 20 nM DS-3′-toe-n and DS-5′-toe-n, Cas12a and crRNA, and 1 × NEBuffer 3.0, recorded by FS5 fluorescence spectrophotometer. **(D)** The real-time fluorescence curve of Cy3 produced by cSDR and CtSDR with different toehold base numbers. 1 μM RP, 0.8 U/μl RNase inhibitor, 100 nM DS-3′-toe-n and DS-5′-toe-n, Cas12a and crRNA, and 1 × NEBuffer 3.0, recorded by 7500 real-time PCR. **(E)** The real-time fluorescence curve of FAM produced by the *trans*-cleavage of CtSDR with different toehold base numbers. Error bars represent the standard deviation of three independent experiments. 1 μM RP, 0.8 U/μl RNase inhibitor, 100 nM DS-3′-toe-n, Cas12a and crRNA, and 1 × NEBuffer 3.0, recorded by 7500 real-time PCR.

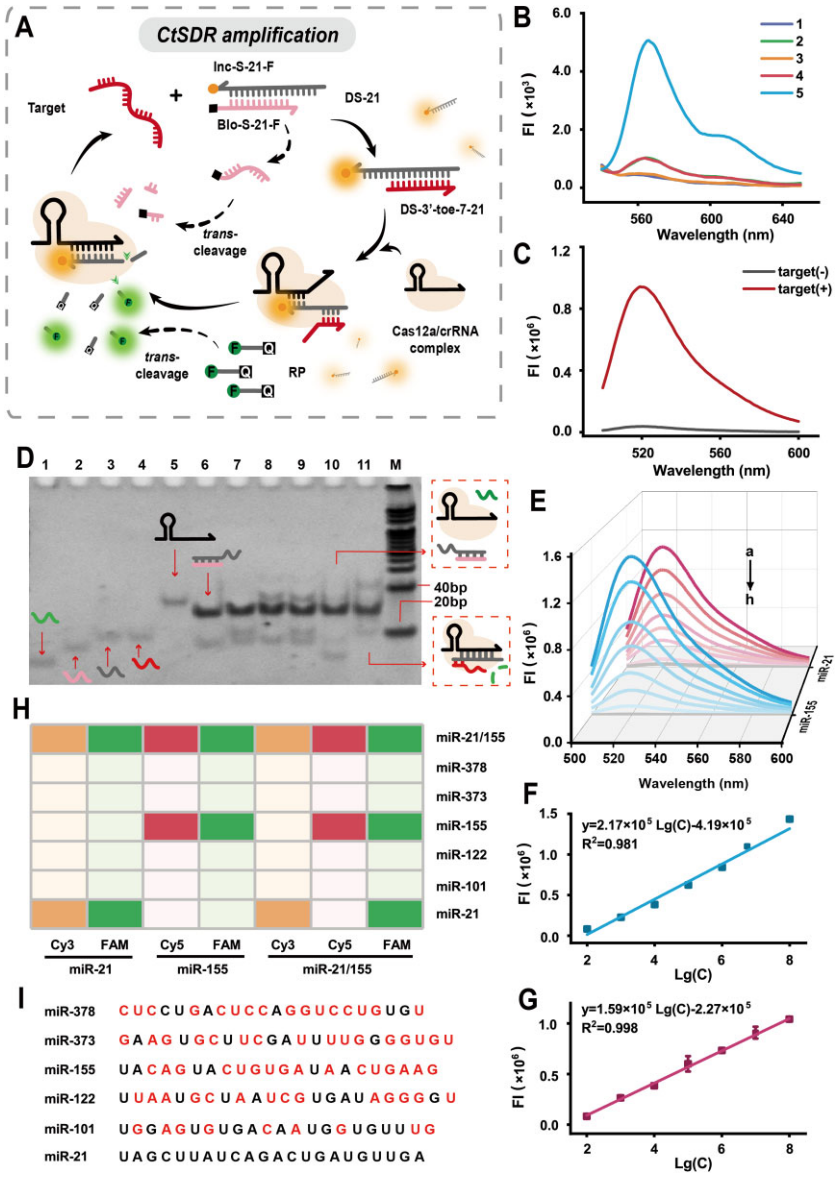

Figure 3. (A) Illustration of target-initiated CtSDR for miRNA detection. **(B)** The FI spectra of target-initiated CtSDR. 1: DS-21, 2: target + DS-21, 3: crRNA + DS-21, 4: target + crRNA + DS-21, 5: target + Cas12a/crRNA complex + DS-21. 200 nM Cas12a, 100 nM crRNA, 100 nM Target, 100 nM DS-21, 0.8 U/μl RNase inhibitor, and 1 × NEBuffer 3.0. **(C)** The *trans*-cleavage fluorescence spectra of target-initiated CtSDR with the target (red line) and without the target (black line). 20 nM Cas12a, 10 nM crRNA, 10 nM Target, 10 nM DS-21, 500 nM RP, 0.8 U/μl RNase inhibitor, and 1 × NEBuffer 3.0. **(D)** 12% PAGE analysis of target-initiated CtSDR. Lane 1: ss-Sub, lane 2: Blo-S-21, lane 3: Inc-S-21, lane 4: target, lane 5: crRNA-21, lane 6: DS-21, lane 7: DS-21 + target, lane 8: DS-21 + crRNA-21, lane 9: DS-21 + crRNA-21 + target, lane 10: DS-21 + crRNA-21 + Cas12a + ss-Sub, and lane 11: DS-21 + crRNA-21 + Cas12a + target + ss-Sub. The concentration of reactants in every lane was 1 μM. **(E)** Typical fluorescence spectra curves responding to 10^8, 10^7, 10^6, 10^5, 10^4, 10^3, 10^2 and 0 fM (from a to h) of different target DNA (blue for miR-155, red for miR-21). The calibration curve for FI versus the logarithm of **(F)** miR-155 and **(G)** miR-21. 20 nM Cas12a, 10 nM crRNA, 10 nM DS-21/DS-155, 500 nM RP, 0.8 U/μl RNase inhibitor and 1 × NEBuffer 3.0. **(H)** Heat map of multiplex detection of miRNAs. The x-axis represents different detection systems and the y-axis represents different miRNAs. 20 nM Cas12a, 10 nM crRNA, 10 nM DS-21/DS-155, 100 nM miRNAs, 500 nM RP, 0.8 U/μl RNase inhibitor and 1 × NEBuffer 3.0. **(I)** The different miRNA sequences. The error bars represent the standard deviation of three independent experiments.

several important experimental parameters, the ratio of Cas to crRNA, reaction buffer and reaction time, were further optimized to upgrade the analytical performance for RNA detection (Supplementary Figure S10). Under the optimized experimental conditions, the analytical performance of the proposed method for multi-target detection was evaluated. As shown in Figure 3E, the FI gradually reduced with a decrease in the target DNA concentration. The linear relationship exhibited in Figure 3F and G indicated a good linear correlation between the FI and the logarithm of the target DNA concentration in the range from 100 fM to 100 nM. The regression equations for miR-21 and miR-155 were $F = 1.59 \times 10^5$ lg (C) – 2.27×10^5 ($R^2 = 0.998$) and F = 2.17×10^5 lg (C) – 4.19×10^5 ($R^2 = 0.981$), respectively, where F represents the FI at 520 nm of FAM and C is the concentration of miR-21 or miR-155. The LOD of miR-21 and miR-155 were calculated according to the 3 σ rule to be 26.8 and 85.6 fM, respectively. Compared with directly using the Cas13a system to detect miR-21 or miR-155, the LOD of miR-21 or miR-155 using our method was enhanced around order of

magnitude (Supplementary Figure S11). Next, the cross-reaction was performed to verify the specificity of the multiplex target-initiated CtSDR. As shown in Figure 3H, adding the corresponding target miRNA activated the SDR (light up Cy3 or Cy5) and further triggered the *trans*-cleavage of Cas12a (light up FAM) in the single target detection system. In the two-target detection system, adding two targets simultaneously recovered the fluorescence of Cy3, Cy5 and FAM, indicating the ability of the proposed method for accurate mutitarget analysis. Other miRNAs (containing miR-21, miR-101, miR-122, miR-155, miR-373 and miR-378) with similar base sequences were also employed to investigate specificity (Figure 3I, Supplementary Table S3). The intuitionistic results suggested that this approach could distinguish different miRNAs from the same family and possesses high specificity. Besides, the reproducibility of our proposed strategy was evaluated on different days. The results showed that the FI maintained stable within 10 days and lightly decreased on the 30th day. And the coefficient of variation (CV) was calculated as 0.06, indicating our method possessed good reproducibility (Supplementary Figure S12). Thus, our proposed strategy offers high sensitivity and specificity for RNA detection and has strong applicability for simultaneous multi-target analysis.

Intra-cellular miRNA monitoring in cultured cells

Prior to evaluating the feasibility of intra-cellular multiplex miRNAs imaging, single-target devices (including DS and Cas12a/crRNA complex) were processed. MCF 7 (a human breast cancer cell line) and MCF 10A (a non-tumorigenic epithelial cell line) cells, which have different miRNA expressions, were explored as a model. Intra-cellular miR-21 and miR-155 were derived to activate the fluorescence of Cy3 (purple) and Cy5 (red) through target-initiated CtSDR, respectively. The fluorescence of FAM (green) was used to ascertain whether miR-21 or miR-155 had initiated *trans*-cleavage of Cas12a. After incubation with single-target devices for MCF 7 and MCF 10A, enhanced fluorescence of Cy3 and Cy5, respectively, was observed compared with the target-initiated cSDR system, suggesting an improvement in SDR efficiency via the proposed target-initiated CtSDR strategy. Bright green fluorescence in the FAM channel implied the feasibility of this method for intra-cellular miRNAs imaging (Figures 4, S13 and S14). Next, a two-target device was implemented to evaluate the feasibility of multiplex miRNAs intra-cellular imaging. As shown in Figure 4, bright Cy3, Cy5 and FAM were all detected in MCF7 cells of the miR-21/miR-155 group, while MCF10A cells showed no fluorescent signals. Flow cytometry further confirmed these results, verifying the feasibility of the intracellular multiplex miRNAs imaging strategy (Figures 4 and S16). Besides, a small reaction volume (10 μl) and no need to wash made this strategy show better discrimination in fluorescence imaging on the slide than in flow cytometry. Compared with the Cas13a system (Supplementary Figure S17), the flow cytometry results showed that the proposed target-initiated CtSDR strategy possessed better specificity in the FAM channel. The fluorescence of cells was also imaged by fluorescence microscopy (Supplementary Figure S15), demonstrating the diverse application scenarios of this method.

The abundance of miRNAs varies across in various physiological processes and under different pathological conditions. It is thus important to sensitively monitor changes in miRNAs in cells to provide useful diagnostic and prognostic information(48). Using miRNA inhibitors and miRNA mimics as regulators, down- or up-regulated miRNA expression levels evaluated via the target-initiated CtSDR system were further examined. Synchronously, the classical technique for evaluating miRNAs levels, i.e. RT-qPCR, was performed to confirm changes in miRNAs levels after treatment with miRNAs inhibitors (Supplementary Table S5). Around a half decrease in fluorescence was observed, indicating the low-expression cell model was successfully built (Supplementary Figure S18). As shown in Figure 4C, the fluorescence intensity in cells treated with either single miRNA inhibitor (miR-21 inhibitor or miR-155 inhibitor) or dual miRNA inhibitors (miR-21/155 inhibitor) exhibited a significant decrease, and the corresponding mean FI levels in every fluorescence channel was significantly lower than that of the negative control (NC) group (Figure 4D). In contrast, when MCF-7 cells were treated with miR-155 mimics to up-regulate the miR-155 expression level, the higher fluorescence intensity in both confocal fluorescence images and RT-qPCR results were observed compared with that observed in the NC group (Supplementary Figure S19). These results reveal that this proposed assay allows simultaneous imaging of changes in the abundance of miRNAs—even at a low expression level—and thus has great potential applications in molecular biology.

Oncogenic RNA rapid imaging of clinical tissue samples

Inspired by the prominent ability of CtSDR to image intracellular miRNAs, we endeavored to explore the potential of target-initiated CtSDR for viral-related oncogenic RNA imaging in tissue. As shown in Figure 5A, the CtSDR-based imaging strategy only had one step for probe hybridization in 1 h, while ISH required more than 14 h, including digoxigenin-labeled probe hybridization, HRP-labeled antibody incubation, DAB reaction and hematoxylin counterstaining. Compared with ISH, the CtSDR-based imaging strategy involves fewer operation steps and has a shorter turnaround time. Moreover, it is worth noting that the DAB used in ISH is carcinogenic and has the potential to induce skin and bladder cancer (49). In contrast, the proposed imaging strategy is DAB-free and more environmentally friendly.

In this section, two small noncoding RNAs Epstein–Barr encoding region EBER-1 and EBER-2, known as EBERs (expresses greater than 10^6 copies per infected cell), was chosen as targets model for imaging the infection situation of the Epstein-Barr virus (EBV) (50). EBV is an oncogenic virus with a high carrier rate in the population and has been closely linked to various malignancies such as nasopharyngeal carcinomas, Hodgkin lymphoma (HL), diffuse large B cell lymphoma (DLB-CL) and Burkitt lymphoma T (51). Therefore, detecting EBERs is important for the diagnosis of EBV infection-related malignancies. To verify the feasibility of CtSDR-based *in situ* imaging strategy for imaging of EBERs (Supplementary Table S6), we used six paraffin-embedded samples of different diseases, in which the first three samples (respectively diagnosed as DLB-CL, classic Hodgkin's lymphoma (CHL) and peripheral T cell lymphoma (PTCL)) were diagnosed as BEER positive and last three samples (Reactive Hyperplasia (RH), Chronic cholecystitis (CP) and Kikuchi disease) were diagnosed as BEERs negative in the clinic. Compared with the last three samples, bright green fluorescence

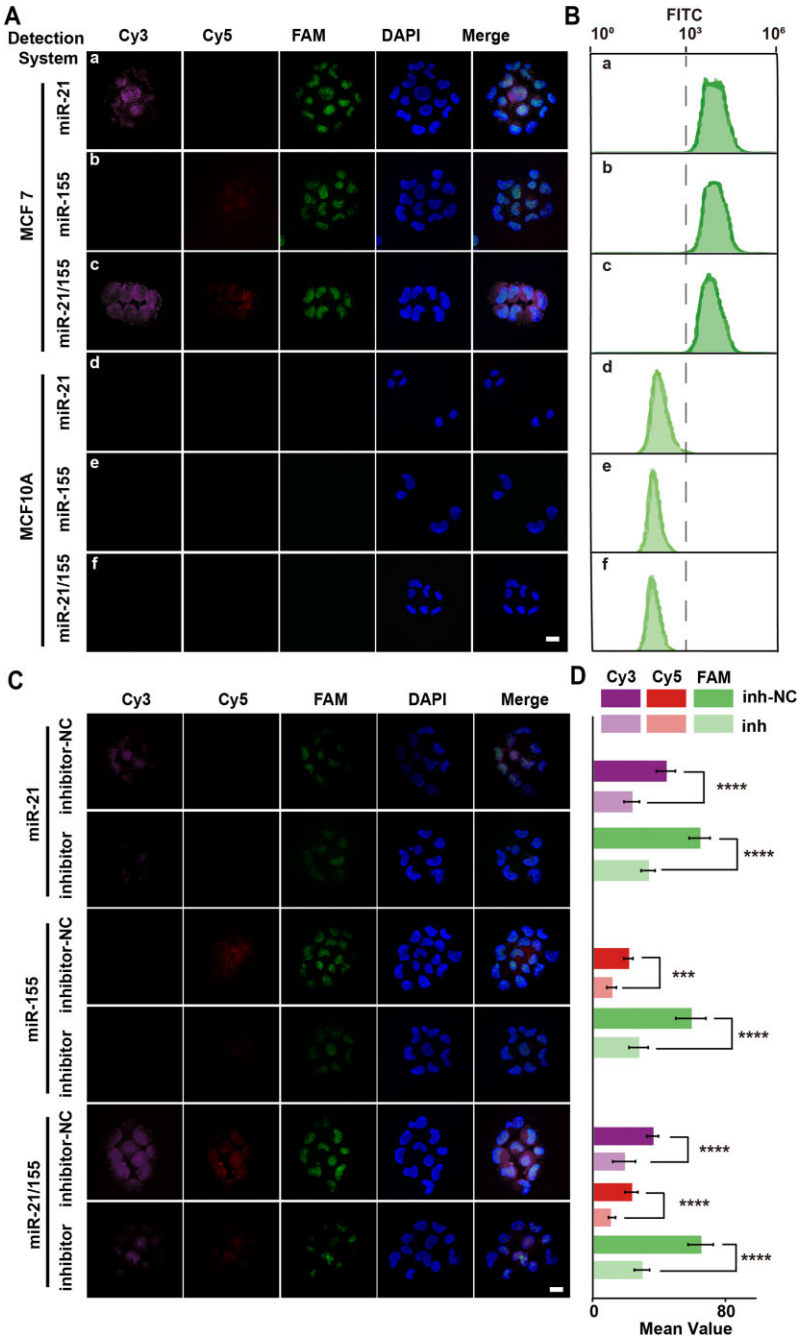

Figure 4. (A) Confocal microscopic images of MCF-7 cells (a to c) and MCF-10A cells (d to f) after incubation with target-initiated CtSDR for simultaneously detecting miR-21 and miR-155. The first column is Cy3 fluorescence with excitation at 556 nm, the second column is Cy5 fluorescence with excitation at 643 nm, the third column is FAM fluorescence with excitation at 492 nm, the fourth column is DAPI fluorescence, and the last column is the merged fluorescence image. Scale bar = 25 μm. 2 μM Cas12a, 1 μM crRNA-21/155, 1 μM DS-21/155, 10 μM RP, 0.8 U/μl RNase inhibitor and 1 × NEBuffer 3.0. **(B)** Flow-cytometry analysis of CtSDR in MCF 7 and MCF 10A. 2 μM Cas12a, 1 μM crRNA-21/155, 1 μM DS-21/155, 10 μM RP, 0.4 U/μl RNase inhibitor and 1 × NEBuffer 3.0. **(C)** Confocal microscopic images of target-initiated CtSDR in MCF-7 cells after treatment with inhibitors and the inhibitor negative control (inhibitor-NC). The first column is Cy3 fluorescence with excitation at 556 nm, the second column is Cy5 fluorescence with excitation at 643 nm, the third column is FAM fluorescence with excitation at 492 nm, the fourth column is DAPI fluorescence, and the last column is the merged fluorescence image. Scale bar = 25 μm. 2 μM Cas12a, 1 μM crRNA-21/155, 1 μM DS-21/155, 10 μM RP, 0.8 U/μl RNase inhibitor and 1 × NEBuffer 3.0. **(D)** The corresponding mean fluorescence value of different groups was calculated using Image J software. Error bars represent the standard deviation of three independent experiments, asterisks indicate *t*-values (***$t < 0.001$, ****$t < 0.0001$). Pictured by TCS SP8 confocal laser scanning microscopy (CLSM, Leica, Germany) with HC PL APO 63×/1.40 oil CS. And the cells used at a density of 1.0×10^6, experiment number = 3.

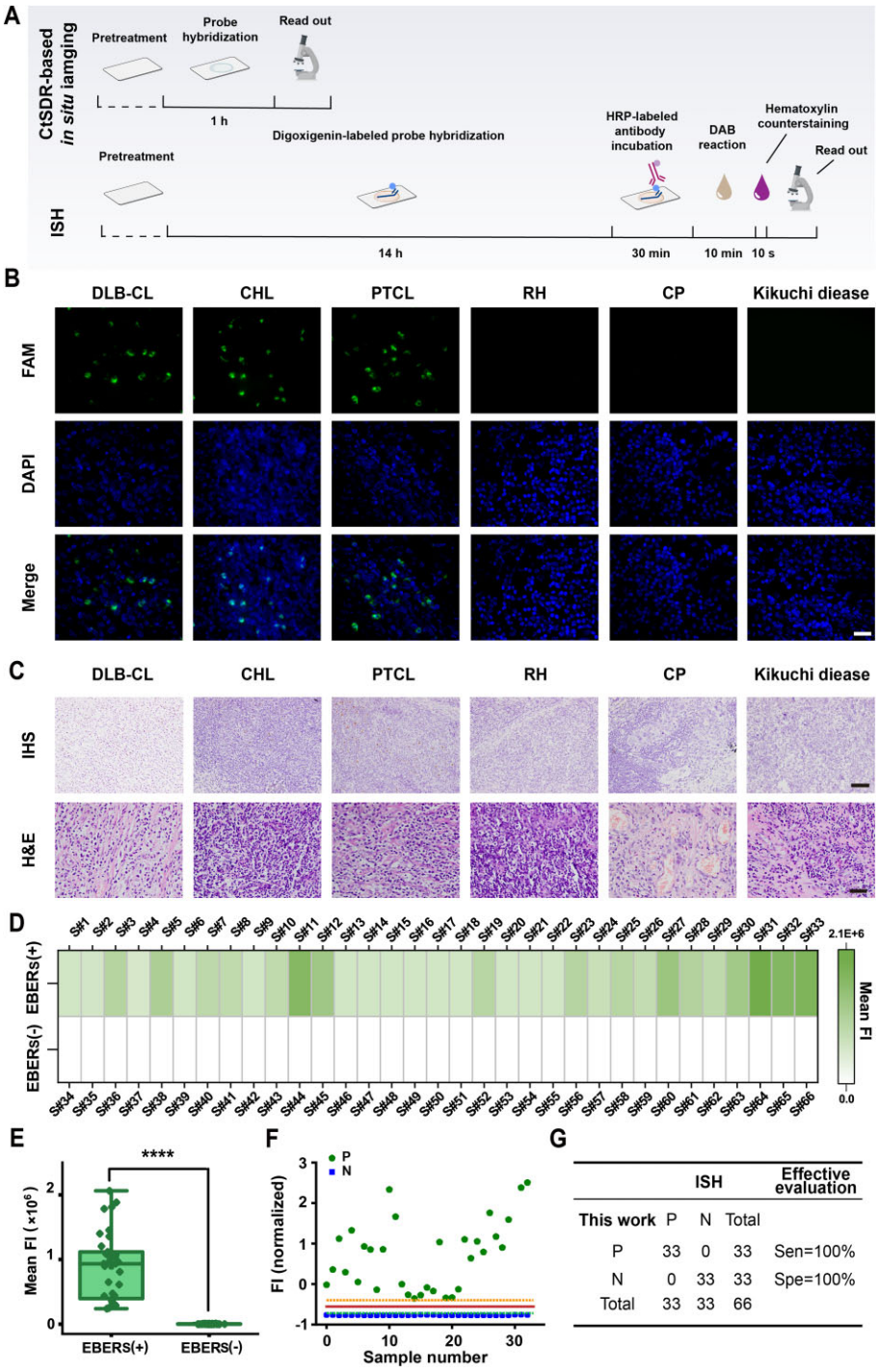

Figure 5. (A) Workflow comparison between the CtSDR-based imaging strategy and traditional ISH. **(B)** Fluorescence microscopic images of tissues after treatment with target-initiated CtSDR. The first row shows FAM fluorescence with excitation at 492 nm, the second row shows DAPI fluorescence, and the last row shows a merged fluorescence image. Scale bar = 80 μm. 2 μM Cas12a, 1 μM crRNA-E1, 1 μM crRNA-E2, 1 μM DS-E1, 1 μM DS-E2, 10 μM RP, 0.8 U/μl RNase inhibitor, and 1 × NEBuffer 3.0. **(C)** ISH and H&E staining of corresponding tissue samples. Scale bar = 100 μm for ISH and bar = 40 μm for H&E staining. The mean FI of 66 clinical samples (including the EBERs (+) group, $n = 33$, and the EBERs (–) group, $n = 33$) was displayed in the heat map **(D)** and box plot **(E)**, asterisks indicate *t*-values (**** $t < 0.0001$). **(F)** The result of SVM learning of normalized FI of 66 samples by CtSDR-based *in situ* imaging strategy, P means positive, N means negative. The decision surface is described by $4.99x + 2.78$ (red line), the decision surface upper is described by -0.39 (orange dashed line) and the decision surface lower is described by –0.71 (green dashed line). **(G)** Efficacy assessment of two methods, CtSDR-based *in situ* imaging, and ISH. P means positive, N means negative, Sen means sensitivity, and Spe means specificity.

was obtained via our method for the first three samples, indicating the feasibility of the CtSDR-based *in situ* imaging strategy for EBERs imaging (Figure 5B). Importantly, these results were consistent with those of ISH, which is the gold standard for EBERs detection, indicating the comparative diagnostic ability of our method. Hematoxylin and eosin (H&E) staining was also performed to assess pathological changes in these six samples (Figure 5C).

Furthermore, a large array ($n = 66$) was employed to evaluate the ability to imaging pathological changes by these three different methods (CtSDR-based *in situ* imaging, ISH and H&E, Supplementary Figures S20, S21 and S22, respectively). ISH was adopted as the gold standard to determine that #1–33 samples were EBERs (+) and #34–66 samples were EBERs (–). Detailed information of these clinical samples and testing data are provided in Supplementary Table S9. Meanwhile, a heat map was generated to summarize the mean FI levels of EBERs expression (Figure 5D). As shown in Figure 5E, the EBERs (+) group had increased mean FI levels in comparison with EBERs (–) group, indicating that the strategy could completely distinguish the expression of EBERs from different diseases. Next, support vector machine (SVM) as the ML algorithm was chosen to carry out classification analysis(52,53). After learning, the decision surface (the red line) was described by $4.99x + 2.78$, in which x means the normalized FI of samples(Figure 5F). The unknown samples could be classified into a positive or negative group based on their normalized FI location relative to the surface (decision surface > 0: positive, decision surface < 0: negative). Moreover, the effective evaluation between CtSDR-based *in situ* imaging and ISH was assessed (Figure 5G). According to the results, our proposed strategy has comparable sensitivity (Sen) and specificity (Spe) with ISH but is superior in terms of detection time.

Based on these results, the proposed CtSDR-based *in situ* imaging strategy for oncogenic RNA has favorable sensitivity and specificity and is superior in terms of detection time and operation steps, supporting its profound practical value for disease diagnosis and prognosis. Thus, this study contributes to the development of advanced imaging techniques for the detection of pathological changes and highlights the potential of CtSDR-based *in situ* imaging as a promising diagnostic tool.

Discussion

Benefited from target-localized cascade signal amplification in the homogeneous phase, SDR has been actively pursued for nucleic acids *in situ* imaging due to its high sensitivity, specificity and fast reaction rate, while the overall efficiency is limited by the energy of the initial reactants and equilibrium of the reaction. The development of a simple, integrated and efficient strategy to overcome the intrinsic limitations of SDR still remains a challenge. In this work, we demonstrated that Cas12a can significantly advance SDR efficiency and delineated the associated mechanism. First, we found that the high affinity of Cas12a towards the substrate thermodynamically drives the SDR equilibrium forward, which can boost the efficiency of the reaction. Second, the *trans*-cleavage of Cas12a drives strand displacement forward by depleting by-products of the reaction. Based on these findings, we proposed an advanced model of strand displacement reaction — CtSDR, which could surmount the limitations of traditional SDR.

We explored the application of target-initiated CtSDR for RNA analysis, which could achieve order of magnitude lower LOD than the Cas13a system. Next, a universal RNA *in situ* imaging platform was developed and applied in cultured cells and paraffin-embedded clinical samples. Given the excellent SDR efficiency, the RNA imaging platform possesses tremendous sensitivity, remarkable specificity and immense potential to monitor RNA expression level changes. The successful localization of oncogenic RNA in clinical tissue samples proves it is a fast and environment-friendly alternative choice for IHS. Besides, despite that the programming ability of the Cas12a effector is limited by protospacer-adjacent motif (PAM) site sequence in many prior studies, CtSDR does not require a PAM site for target recognition, expanding the application mode of Cas12a programming. These advantages enable CtSDR promising clinical applications, especially in the field of disease diagnosis.

In summary, this new CtSDR method, with its mechanisms radically investigated and its applications comprehensively verified, may inspire new techniques for molecular diagnosis, such as *in situ* imaging. This work provides a deeper understanding of Cas12a and broader application scenarios for both SDR and the CRISPR/Cas system.

Data availability

The data that support the findings of this study are available within the article and its Supplementary Information files or from the corresponding author upon reasonable request.

Supplementary data

Supplementary Data are available at NAR Online.

Funding

National Natural Science Foundation of China [82372334, 81873972]; Chongqing Science Fund for Distinguished Young Scholars [cstc2019jcyjjqX0028]; Foundation for Innovative Research Groups of Chongqing Higher Education Institutions [CXQT20013]; Chongqing Talents-Innovation Leading Talents Project [CQYC20200303107, cstc2022ycjh-bgzxm0001]; Natural Science Foundation of Chongqing [Postdoctoral Foundation, cstc2021jcyj-bsh X0153]; First-class discipline construction project of clinical medicine in the First Clinical College of Chongqing Medical University [472020320220007].

Conflict of interest statement

None declared.

References

1. Bueno,M.J. and Malumbres,M. (2011) MicroRNAs and the cell cycle. *Biochim. Biophys. Acta*, **1812**, 592–601.
2. Martinez-Ledesma,E., Verhaak,R.G.W. and Treviño,V. (2015) Identification of a multi-cancer gene expression biomarker for cancer clinical outcomes using a network-based algorithm. *Sci. Rep.*, **5**, 11966.
3. Hrašovec,S. and Glavač,D. (2012) MicroRNAs as novel biomarkers in colorectal cancer. *Front. Genet.*, **3**, 180.
4. Pritchard,C.C., Cheng,H.H. and Tewari,M. (2012) MicroRNA profiling: approaches and considerations. *Nat. Rev. Genet.*, **13**, 358–369.

5. Válóczi,A., Hornyik,C., Varga,N., Burgyán,J., Kauppinen,S. and Havelda,Z. (2004) Sensitive and specific detection of microRNAs by northern blot analysis using LNA-modified oligonucleotide probes. *Nucleic Acids Res.*, **32**, e175.
6. Berezikov,E., Cuppen,E. and Plasterk,R.H.A. (2006) Approaches to microRNA discovery. *Nat. Genet.*, **38**, S2–S7.
7. Duan,D., Zheng,K., Shen,Y., Cao,R., Jiang,L., Lu,Z., Yan,X. and Li,J. (2011) Label-free high-throughput microRNA expression profiling from total RNA. *Nucleic Acids Res.*, **39**, e154.
8. Baker,M. (2010) MicroRNA profiling: separating signal from noise. *Nat. Methods*, **7**, 687–692.
9. Yin,J.Q., Zhao,R.C. and Morris,K.V. (2008) Profiling microRNA expression with microarrays. *Trends Biotechnol.*, **26**, 70–76.
10. Hung,J.-H. and Weng,Z. (2017) Analysis of microarray and RNA-seq expression profiling data. *Cold Spring Harb. Protoc.*, **2017**, pdb.top093104.
11. Yang,F., Lu,H., Meng,X., Dong,H. and Zhang,X. (2022) Shedding light on DNA-based nanoprobes for live-cell microRNA imaging. *Small*, **18**, e2106281.
12. Xiao,Y., Wang,X., Zhang,H., Ulintz,P.J., Li,H. and Guan,Y. (2020) FastClone is a probabilistic tool for deconvoluting tumor heterogeneity in bulk-sequencing samples. *Nat. Commun.*, **11**, 4469.
13. Le,P., Ahmed,N. and Yeo,G.W. (2022) Illuminating RNA biology through imaging. *Nat. Cell Biol.*, **24**, 815–824.
14. Braselmann,E., Rathbun,C., Richards,E.M. and Palmer,A.E. (2020) Illuminating RNA biology: tools for imaging RNA in live mammalian cells. *Cell Chem Biol*, **27**, 891–903.
15. Braselmann,E., Wierzba,A.J., Polaski,J.T., Chromiński,M., Holmes,Z.E., Hung,S.-T., Batan,D., Wheeler,J.R., Parker,R., Jimenez,R., *et al.* (2018) A multicolor riboswitch-based platform for imaging of RNA in live mammalian cells. *Nat. Chem. Biol.*, **14**, 964–971.
16. Tao,Y., Zhou,X., Sun,L., Lin,D., Cai,H., Chen,X., Zhou,W., Yang,B., Hu,Z., Yu,J., *et al.* (2023) Highly efficient and robust π-FISH rainbow for multiplexed in situ detection of diverse biomolecules. *Nat. Commun.*, **14**, 443.
17. Wang,F., Flanagan,J., Su,N., Wang,L.-C., Bui,S., Nielson,A., Wu,X., Vo,H.-T., Ma,X.-J. and Luo,Y. (2012) RNAscope: a novel in situ RNA analysis platform for formalin-fixed, paraffin-embedded tissues. *J. Mol. Diagn.*, **14**, 22–29.
18. Rouhanifard,S.H., Mellis,I.A., Dunagin,M., Bayatpour,S., Jiang,C.L., Dardani,I., Symmons,O., Emert,B., Torre,E., Cote,A., *et al.* (2019) ClampFISH detects individual nucleic acid molecules using click chemistry–based amplification. *Nat. Biotechnol.*, **37**, 84–89.
19. Dardani,I., Emert,B.L., Goyal,Y., Jiang,C.L., Kaur,A., Lee,J., Rouhanifard,S.H., Alicea,G.M., Fane,M.E., Xiao,M., *et al.* (2022) ClampFISH 2.0 enables rapid, scalable amplified RNA detection in situ. *Nat. Methods*, **19**, 1403–1410.
20. Zhang,D.Y. and Seelig,G. (2011) Dynamic DNA nanotechnology using strand-displacement reactions. *Nat. Chem.*, **3**, 103–113.
21. Peng,H., Newbigging,A.M., Reid,M.S., Uppal,J.S., Xu,J., Zhang,H. and Le,X.C. (2020) Signal amplification in living cells: a review of microRNA detection and imaging. *Anal. Chem.*, **92**, 292–308.
22. Qian,L. and Winfree,E. (2011) Scaling up digital circuit computation with DNA strand displacement cascades. *Science*, **332**, 1196–1201.
23. Cherry,K.M. and Qian,L. (2018) Scaling up molecular pattern recognition with DNA-based winner-take-all neural networks. *Nature*, **559**, 370–376.
24. Yurke,B., Turberfield,A.J., Mills,A.P., Simmel,F.C. and Neumann,J.L. (2000) A DNA-fuelled molecular machine made of DNA. *Nature*, **406**, 605–608.
25. Shi,K., Dou,B., Yang,C., Chai,Y., Yuan,R. and Xiang,Y. (2015) DNA-fueled molecular machine enables enzyme-free target recycling amplification for electronic detection of microRNA from cancer cells with highly minimized background noise. *Anal. Chem.*, **87**, 8578–8583.
26. Yang,F., Cheng,Y., Cao,Y., Dong,H., Lu,H., Zhang,K., Meng,X., Liu,C. and Zhang,X. (2019) Sensitively distinguishing intracellular precursor and mature microRNA abundance. *Chem. Sci.*, **10**, 1709–1715.
27. Wu,H., Chen,T.-T., Wang,X.-N., Ke,Y. and Jiang,J.-H. (2020) RNA imaging in living mice enabled by an *in vivo* hybridization chain reaction circuit with a tripartite DNA probe. *Chem. Sci.*, **11**, 62–69.
28. Bi,S., Yue,S. and Zhang,S. (2017) Hybridization chain reaction: a versatile molecular tool for biosensing, bioimaging, and biomedicine. *Chem. Soc. Rev.*, **46**, 4281–4298.
29. Liu,J., Zhang,Y., Xie,H., Zhao,L., Zheng,L. and Ye,H. (2019) Applications of catalytic hairpin assembly reaction in biosensing. *Small*, **15**, e1902989.
30. Zhu,D., Huang,J., Lu,B., Zhu,Y., Wei,Y., Zhang,Q., Guo,X., Yuwen,L., Su,S., Chao,J., *et al.* (2019) Intracellular microRNA imaging with MoS_2-supported nonenzymatic catassembly of DNA hairpins. *ACS Appl. Mater. Inter.*, **11**, 20725–20733.
31. Karunanayake Mudiyanselage,A.P.K.K., Yu,Q., Leon-Duque,M.A., Zhao,B., Wu,R. and You,M. (2018) Genetically encoded catalytic hairpin assembly for sensitive RNA imaging in live cells. *J. Am. Chem. Soc.*, **140**, 8739–8745.
32. Srinivas,N., Ouldridge,T.E., Sulc,P., Schaeffer,J.M., Yurke,B., Louis,A.A., Doye,J.P.K. and Winfree,E. (2013) On the biophysics and kinetics of toehold-mediated DNA strand displacement. *Nucleic Acids Res.*, **41**, 10641–10658.
33. Gao,M., Daniel,D., Zou,H., Jiang,S., Lin,S., Huang,C., Hecht,S.M. and Chen,S. (2018) Rapid detection of a dengue virus RNA sequence with single molecule sensitivity using tandem toehold-mediated displacement reactions. *Chem. Commun. (Camb.)*, **54**, 968–971.
34. Green,S.J., Lubrich,D. and Turberfield,A.J. (2006) DNA hairpins: fuel for autonomous DNA devices. *Biophys. J.*, **91**, 2966–2975.
35. Li,X., Xie,J., Jiang,B., Yuan,R. and Xiang,Y. (2017) Metallo-toehold-activated catalytic hairpin assembly formation of three-way DNAzyme junctions for amplified fluorescent detection of Hg2. *Acs Appl Mater Inter*, **9**, 5733–5738.
36. Hata,H., Kitajima,T. and Suyama,A. (2018) Influence of thermodynamically unfavorable secondary structures on DNA hybridization kinetics. *Nucleic Acids Res.*, **46**, 782–791.
37. Zhang,D., Yan,Y., Cheng,X., Yang,T., Li,X., Ding,S., Zhang,X. and Cheng,W. (2022) Controlling the trans-cleavage of CRISPR-Cas12a with nicked PAM: universal platform for biosensing. *Sensor Actuat. B-Chem.*, **353**, 131153.
38. Kaminski,M.M., Abudayyeh,O.O., Gootenberg,J.S., Zhang,F. and Collins,J.J. (2021) CRISPR-based diagnostics. *Nat Biomed Eng*, **5**, 643–656.
39. Mao,S., Ying,Y., Wu,X., Krueger,C.J. and Chen,A.K. (2019) CRISPR/dual-FRET molecular beacon for sensitive live-cell imaging of non-repetitive genomic loci. *Nucleic Acids Res.*, **47**, e131.
40. Chen,J.S., Ma,E., Harrington,L.B., Da Costa,M., Tian,X., Palefsky,J.M. and Doudna,J.A. (2018) CRISPR-Cas12a target binding unleashes indiscriminate single-stranded DNase activity. *Science*, **360**, 436–439.
41. Simmel,F.C., Yurke,B. and Singh,H.R. (2019) Principles and applications of nucleic acid strand displacement reactions. *Chem. Rev.*, **119**, 6326–6369.
42. Swarts,D.C., van der Oost,J. and Jinek,M. (2017) Structural basis for guide RNA processing and seed-dependent DNA targeting by CRISPR-Cas12a. *Mol. Cell*, **66**, 221–233.
43. Strohkendl,I., Saifuddin,F.A., Rybarski,J.R., Finkelstein,I.J. and Russell,R. (2018) Kinetic basis for DNA target specificity of CRISPR-Cas12a. *Mol. Cell*, **71**, 816–824.
44. Balderston,S., Taulbee,J.J., Celaya,E., Fung,K., Jiao,A., Smith,K., Hajian,R., Gasiunas,G., Kutanovas,S., Kim,D., *et al.* (2021) Discrimination of single-point mutations in unamplified genomic DNA via Cas9 immobilized on a graphene field-effect transistor. *Nat. Biomed. Eng.*, **5**, 713–725.

45. Yang,H., Chen,J., Yang,S., Zhang,T., Xia,X., Zhang,K., Deng,S., He,G., Gao,H., He,Q., *et al.* (2021) CRISPR/Cas14a-based isothermal amplification for profiling plant microRNAs. *Anal. Chem.*, **93**, 12602–12608.
46. Zhang,D.Y. and Winfree,E. (2009) Control of DNA strand displacement kinetics using toehold exchange. *J. Am. Chem. Soc.*, **131**, 17303–17314.
47. APM,J. and Yurke,B. (2003) Using DNA to power nanostructures. *Genet. Programm. Evolvable Mach.*, **4**, 111–122.
48. Sato,H., Das,S., Singer,R.H. and Vera,M. (2020) Imaging of DNA and RNA in living eukaryotic cells to reveal spatiotemporal dynamics of gene expression. *Annu. Rev. Biochem.*, **89**, 159–187.
49. Thomas,N.S., George,K. and Namasivayam,N. (2016) Molecular aspects and chemoprevention of dimethylaminoazobenzene-induced hepatocarcinogenesis: a review. *Hepatol Res*, **46**, 72–88.
50. Weiss,L.M. and Chen,Y.-Y. (2013) EBER in situ hybridization for Epstein-Barr virus. *Methods Mol. Biol.*, **999**, 223–230.
51. Fournier,B., Boutboul,D., Bruneau,J., Miot,C., Boulanger,C., Malphettes,M., Pellier,I., Dunogué,B., Terrier,B., Suarez,F., *et al.* (2020) Rapid identification and characterization of infected cells in blood during chronic active Epstein-Barr virus infection. *J. Exp. Med.*, **217**, e20192262.
52. Lin,C.-F. and Wang,S.-D. (2002) Fuzzy support vector machines. *IEEE Trans. Neural Netw.*, **13**, 464–471.
53. Wang,T., Shao,W., Huang,Z., Tang,H., Zhang,J., Ding,Z. and Huang,K. (2021) MOGONET integrates multi-omics data using graph convolutional networks allowing patient classification and biomarker identification. *Nat. Commun.*, **12**, 3445.

Received: May 30, 2023. **Revised:** October 9, 2023. **Editorial Decision:** October 11, 2023. **Accepted:** October 12, 2023